ACS Combinatorial Science

Research Article

Cite This: ACS Comb. Sci. 2018, 20, 633−642

pubs.acs.org/acscombsci

Combinatorial Thin Film Sputtering Au_xAl_{1-x} Alloys: Correlating Composition and Structure with Optical Properties

Robyn Collette,[†] Yueying Wu,[‡] Agust Olafsson,[‡] Jon P. Camden,[‡] and Philip D. Rack*[,†,§]

[†]Department of Materials Science and Engineering, University of Tennessee, Knoxville, Tennessee 37996, United States

[‡]Department of Chemistry and Biochemistry, University of Notre Dame,Notre Dame, Indiana 46556, United States

[§]Center for Nanophase Materials Science, Oak Ridge National Laboratory, Oak Ridge, Tennessee 37831, United States

Supporting Information

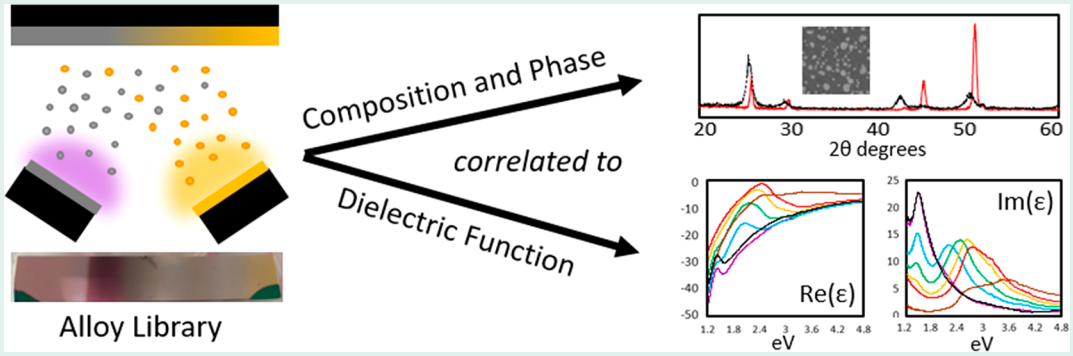

ABSTRACT: The Au−Al alloy system was investigated via a combinatorial thin film sputtering method for its potential as a plasmonic material. Au_xAl_{1-x} combinatorial libraries were cosputtered from Au and Al elemental targets and the composition, phase, and dielectric function of a ∼350 nm film was determined using energy dispersive spectroscopy (EDS), grazing incidence X-ray diffraction (GIXRD), and spectroscopic ellipsometry, respectively. The phase evolution and optical properties were analyzed after annealing various compositions under a vacuum. The phases present matched the expected phases based on the published Al−Au binary phase diagram at all compositions. Interestingly, the mixed phase Al-$AuAl_2$ region showed the most optical tunability, where a maximum in the real part of the dielectric function progressively shifted to higher energy for increasing gold concentration. For almost pure $AuAl_2$, the imaginary component is largely reduced in the visible range and is comparable to that of pure Al in the UV region. A 20-nm-thick film with composition $Au_{0.74}Al_{0.26}$ was studied using a (scanning) transmission electron microscope with an *in situ* laser heating system. The structures of the as-deposited and laser annealed films were determined using selected area diffraction and the bulk plasmon of $AuAl_2$ and Al realized with electron energy loss spectroscopy. Last, the Au-rich solid solution region was investigated as a surface enhanced Raman spectroscopy (SERS) substrate using the benezenethiol (BT) molecule. Good SERS intensity was maintained up to 30% Al addition where enhancements of 10^5 to 10^7 were still observed.

KEYWORDS: *combinatorial sputtering, thin film, plasmonic, alloy*

INTRODUCTION

Rapid synthesis of thin film material libraries is critical for developing many solid state material solutions. To this end, our group has employed a combinatorial thin film sputtering method to synthesize material libraries. The system is equipped with four individual sputtering sources with adjustable tilt, which can be used to adjust the compositional gradient of the combinatorial library. Our system has been exploited to explore various thin film materials ranging from catalytic,[1,2] magnetic,[3,4] optical,[5−12] electrical,[13] mechanical,[3,14−16] and radiation hard materials.[17,18] Other groups have employed similar approaches to combinatorial thin films. Prominent groups have explored, for example, catalytic,[19−22] bulk metallic glass,[23] magnetic,[24,25] optical,[26−28] electrical,[28−31] and mechanical[32] materials. Additionally, a few reviews on the subject have been published.[33−36] Mixed metallic alloys are an important means to tune the plasmon resonance or combine plasmonic properties with other functionalities,[37] which may be superior to that of the individual elements. Using combinatorial approaches, Gong et al. for instance, found that $Ag_{0.5}Au_{0.5}$, $Au_{0.1}Cu_{0.9}$, and $Cu_{0.1}Ag_{0.9}$ have lower optical losses and exhibited enhanced surface plasmon polariton lengths in certain optical regions relative to individual elements.[27] Au−Ag alloys have been shown to combine the stability of Au with the superior properties of Ag.[38] Others have shown that 5% Zn addition enhances the oxidation

Received: July 2, 2018
Revised: September 27, 2018
Published: October 2, 2018

DOI: 10.1021/acscombsci.8b00091
ACS Comb. Sci. 2018, 20, 633−642

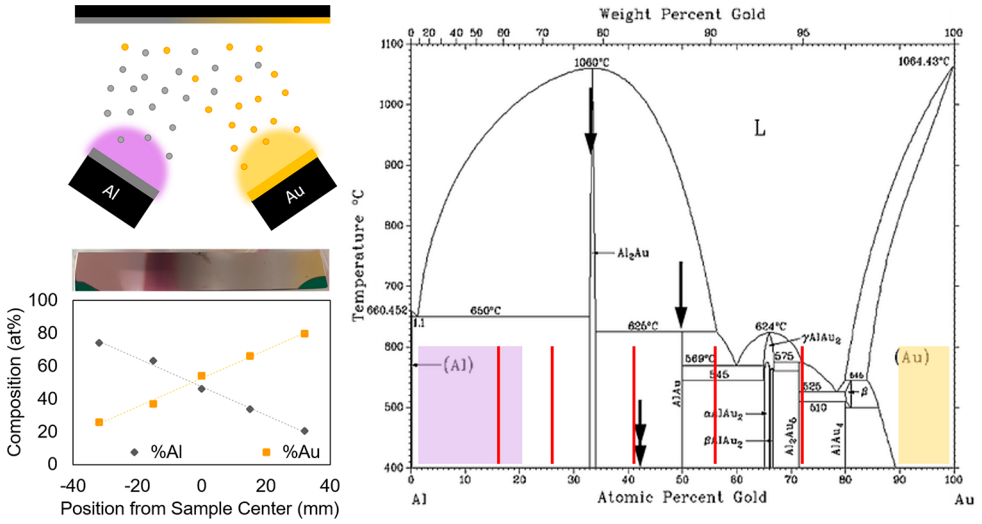

Figure 1. Schematic illustrating combinatorial sputtering arrangement to achieve a compositional gradient across a sample. Binary Au−Al phase diagram[47] with red lines corresponding to the initial compositions studied, and the subsequent regions that were studied highlighted in gold (corresponding to Au-rich solid solution region of the phase diagram) and purple (corresponding to the Al-AuAl2 mixed phase region).

Table 1. Sputter Deposition Parameters

	target power (W)			approximate deposition rate (nm/min)		
composition	Al	Au	deposition time (hr:min)	Al	Au	composition gradient (Δx/mm)
pure Au	0	40	1:40	0	3.3	
pure Al	200	0	1:40	3.5	0	
$0.15 < x < 0.72$	100	20	1:40	2.0	1.5	0.006
$0.9 < x < 1.0$	30	40	1:27	1.1	3.3	0.001
$0 < x < 0.2$	200	10	1:20	3.5	0.25	0.002

resistance of Cu.[39] Because of the vast composition space needed to be explored, combinatorial approaches can facilitate research into multicomponent alloys for advanced plasmonic applications. The dielectric properties of a number of alloy systems, such as Au−Ag,[27,40] Ag−Cu,[27,41] and Au−Cu,[27] have been examined using optical spectroscopy and more recently the Au−Ag system by both ellipsometry and electron energy loss spectroscopy (EELS).[5] The correlation of the dielectric properties with alloy composition not only reveals interesting physics but also facilitates the rationale design and synthesis of alloy plasmonic nanostructures. Among various plasmon active alloys, the Au_xAl_{1-x} system is potentially interesting due to the fact that elemental Au[42] and Al[43] have strong plasmon resonances in the visible and ultraviolet (UV) regions, respectively. Thus, the capability of tuning the plasmon resonance from the visible to the UV region via Au_xAl_{1-x} alloys for low loss plasmonic applications is intriguing. Indeed, the potential importance of $AuAl_2$ as a plasmonic material has been suggested both theoretically and experimentally.[44,45] Furthermore, the effect of Al additions on the optical properties of Au has been explored previously.[46] However, a systematic study of the complete Au_xAl_{1-x} system which correlates the phases present and optical properties is lacking.

In this study, we leverage a combinatorial thin film cosputtering approach to rapidly synthesize a Au_xAl_{1-x} library.[9] Several critical points on the phase diagram are targeted, and the phase evolution of the as-deposited and annealed films are correlated to the resultant dielectric functions. The alloy composition and phase structures are analyzed using energy dispersive X-ray spectroscopy (EDS) and grazing incidence X-ray diffraction (GIXRD), respectively. The dielectric constant as a function of energy is measured via spectroscopic ellipsometry. The phase evolution of the $Au_{0.26}Al_{0.74}$ composition is determined via *in situ* laser annealing in the transmission electron microscope and correlated to the low-loss electron energy loss spectroscopy, correlating the plasmonic properties to the evolving microstructure. Finally, the Au-rich region of the phase diagram was tested as a SERS substrate for rhodamine-6G and benzenethiol molecules.

EXPERIMENTAL PROCEDURES

Au−Al Alloy Thin Film Synthesis. Au_xAl_{1-x} alloy films ~350 nm thick were sputter deposited by RF magnetron sputtering onto 100 mm × 15 mm polished [100] silicon substrates or onto 5 μm of thermally grown SiO_2. The alloys were deposited by cosputtering pure Au and Al elemental targets, which were confocally directed toward the substrate as demonstrated in Figure 1. The substrates were positioned such that one end was closer to the Au target and the other closer to the Al target; thus, a composition gradient across the long axis of the sample was realized. The RF power supplied to each target is summarized in Table 1 for each gradient of interest. Several samples of each composition gradient were deposited as various annealing conditions were explored to correlate the phase evolution to the observed optical properties. For the $0.15 < x < 0.72$ composition gradient, the samples were subsequently annealed under a vacuum for 30 min at 100 °C, 300 °C, and 500 °C, and for the $0 < x < 0.2$ and $0.9 < x < 1$ composition gradients, as-deposited and 500 °C annealed samples were investigated.

DOI: 10.1021/acscombsci.8b00091
ACS Comb. Sci. 2018, 20, 633−642

Composition Measurement by EDS. The chemical composition of the film was measured at several locations along the sample for each gradient variety using a scanning electron microscope (Zeiss Evo) equipped with an energy dispersive X-ray spectroscopy detector (Bruker XFlash 6130). The spot size was around 1 μm × 1 μm. The accelerating voltage was set to 10 keV to record the spectra, which allowed for observation of Al (Kα 1.486 keV)[48] and Au (Mα 2.123 keV)[48] peaks for quantification. The recorded compositions were plotted as a function of sample position and used for determining spot locations in subsequent measurements. The change in composition per millimeter for each sample is reported in Table 1. All subsequent measurements have a sufficiently small spot size such that the composition within the spot is approximately constant.

Phase Region Analysis. Grazing incidence X-ray diffraction (Panalytical X'Pert3MRD) was used to measure the crystallographic structure of the films within a 4 mm × 9 mm region. Note that the composition on the sample was nonuniform along the 4 mm direction but was uniform in the 9 mm direction. The density of the film was approximated as an average of that of Au and Al and used to calculate the approximate penetration depth of the incident X-ray beam as a function of angle. The incidence angle for measurement was chosen to be 1.2° with an approximate penetration depth of 400 nm, thus allowing the measurement to probe the film only and to prevent substrate effects. The diffracted beam intensity was recorded over 20° to 60°, a range which contained the main peaks for all Au−Al alloy compositions we would expect. Peaks were analyzed using Panalytical HighScore Plus software.

Determination of Dielectric Function of Alloyed Films. The dielectric function was measured using a J. A. Woolam M-2000U variable-angle spectroscopic ellipsometer over wavelengths between 245 and 999 nm with a spot size of 4 mm × 8 mm. The dielectric function of an alloy film was calculated from the ellipsometrically measured Ψ (Psi) and Δ (Delta), which is a measurement of the change in polarization of the incident beam when it interacts with the alloy film. Because the alloy films are all optically thick and smooth, $R(\varepsilon)$ and $\mathrm{Im}(\varepsilon)$ were obtained by point-by-point fitting of the calculated data. No dispersion model was used to fit the result, considering there is no existing model suited perfectly for the polycrystalline alloy films in our case due to complex phase structure, crystalline size, and energy band composition in each alloy. The measurements were performed at a fixed angle (65°) after preliminary test measurements were done at different angles and yielded consistent results.

TEM and EELS Experiment. $Au_{0.26}Al_{0.74}$ was sputtered to a thickness of ∼20 nm onto a 20-nm-thick SiO_2 TEM membrane using a monochromated Carl Zeiss LIBRA 200MC (S)TEM with an operating voltage of 200 kV. TEM images were taken at 31.5 kX. A 20 μm aperture was used for the as-deposited SAED and a 5 μm aperture for the annealed area. SAED images were radially averaged using a rotational averaging script[20] within Gatan Digital Micrograph. The STEM images were performed with a convergence semiangle of 10 mrad and a collection semiangle of 15 mrad. The low loss spectra were collected with a slit of 0.5 μm, and a dispersion of 29 meV per channel. The measured energy resolution (defined as the full width at half-maximum of the zero-loss peak) is 180 meV with the electron beam penetrating the SiO_2 substrate only. For the spectrum image in Figure 9, a ROI was chosen as 6 × 16 pixel spectra (1 pixel ∼ 10 nm × 10 nm) for c, 18 × 22 pixel spectra (1 pixel ∼ 10 nm × 10 nm) for the top panel in g, and 7 × 27 pixel spectra (1 pixel ∼ 10 nm × 10 nm) for the middle and bottom panels in g. The bulk plasmon maps in Figure 9c and g were obtained by plotting spectra intensity in designated energy slices. The point EEL spectra in Figure 9h were normalized to zero-loss peak (ZLP), and the background spectrum was subtracted.

SERS Sample Preparation and Measurement. Si [100] wafers were cut into 5 mm × 5 mm size pieces. The unpolished backside of Si [100] 5 mm × 5 mm wafers were irradiated using a KrF excimer laser (248 nm, 18 ns) with an energy density of 2 J/cm^2 to create a textured surface. Au_xAl_{1-x} (x = 0.76, 0.81, 0.88, 0.96) films were sputtered to a thickness of 200 nm on the surface using the combinatorial sputtering system described above. A lab-built Raman spectrometer (HeNe 633 nm, Thorlabs) was used to collect spectra under ambient conditions. The beam was focused onto the sample (typical power 65 μW) using an inverted microscope objective (Nikon 20x, NA = 0.5). Scattered light was collected in the same objective, passed through a Rayleigh rejection filter (Semrock), and dispersed in a spectrometer (PI Acton Research, f = 0.3 m, 1200 grooves per mm). Light is detected by a back illuminated deep-depletion CCD (PIXIS, Spec-10, Princeton Instruments). Winspec 32 software (Princeton Instruments) operates the CCD and spectrometer. SERS spectra were collected in 5 s acquisitions, for a total time of 60 s at three regions of interest per Au_xAl_{1-x} substrate.

RESULTS AND DISCUSSION

Investigation of Compositions 0.15 < x < 0.72. Au_xAl_{1-x} alloys of compositions ranging 0.15 < x < 0.72 were initially investigated, and the experimentally measured dielectric functions were correlated to the phase structures of as-deposited and annealed alloys at specific compositions. The compositions that were specifically examined were x = 0.16, 0.26, 0.41, 0.56, and 0.72. The GIXRD of the as-deposited and 500 °C/30 min anneal patterns are shown in Figure 2, and the phases identified at each sample composition are summarized in Table 2 with the dominant phase in bold. The real and imaginary part of the dielectric function as a function of energy for each as-deposited and annealed composition is shown in Figure 3.

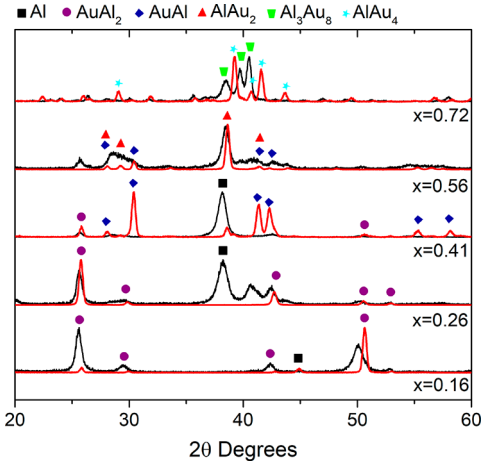

Figure 2. GIXRD results for Au_xAl_{1-x} film samples. As-deposited samples shown in black while annealed samples are shown in red.

DOI: 10.1021/acscombsci.8b00091
ACS Comb. Sci. 2018, 20, 633−642

Table 2. Phases Present in 0.15< x < 0.72 Films Determined by GIXRD with Primary Phases in Bold Print

	distance from sample center (mm) and chemical composition				
anneal condition	−32 $Au_{0.16}Al_{0.84}$	−15 $Au_{0.26}Al_{0.74}$	0 $Au_{0.41}Al_{0.59}$	15 $Au_{0.56}Al_{0.44}$	32 $Au_{0.72}Al_{0.28}$
as deposited	Al, $AuAl_2$	Al, $AuAl_2$, AuAl	$AlAu_2$, $AuAl_2$, Al	$AlAu_2$, Al_3Au_8	Al_3Au_8
500 ° C anneal	Al, **$AuAl_2$**	**$AuAl_2$**	AuAl, $AlAu_2$	**$AlAu_2$**, Al_3Au_8	**$AlAu_4$**, Al_3Au_8

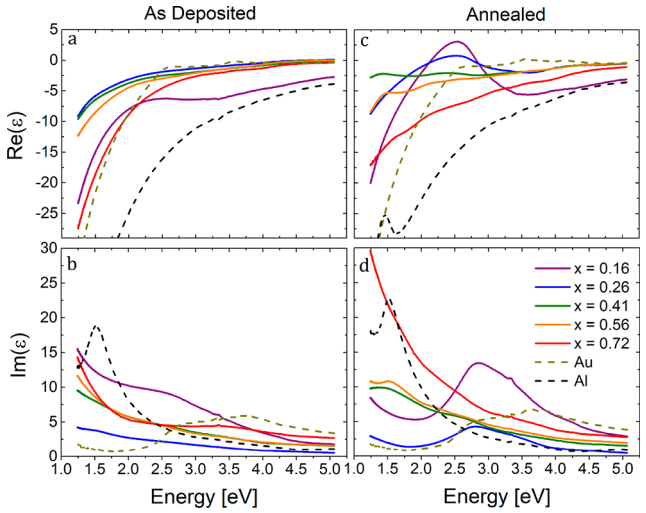

Figure 3. Dielectric function for Au_xAl_{1-x} film samples. Real (a) and imaginary (b) components of the dielectric function of the as-deposited sample in the first column and the real (c) and imaginary (d) components for the annealed sample in the second column.

For the composition where x = 0.72, the equilibrium phase diagram suggests that a mixture of Al_2Au_5 and $AlAu_4$ should be present. While many equilibrium phase diagrams suggest the composition Al_2Au_5, it has however since been shown that the Al_2Au_5 phase is actually Al_3Au_8,[49] although both continue to be used in the literature. GIXRD suggests that the as-deposited samples contain primarily Al_3Au_8. However, upon annealing, $AuAl_4$ becomes the dominant phase with some Al_3Au_8 reflections remaining. This agrees well with Manji et al. where they showed that Al_2Au_5 (really Al_3Au_8) is the first compound to form at the interface in bilayer Au−Al films deposited and aged at room temperature.[50,51]

At x = 0.56, we expect a mixture of AuAl and $AlAu_2$, and these are in fact the reflections observed in the as-deposited sample. Subsequent to annealing, the $AlAu_2$ emerges as the dominant phase. The Au_xAl_{1-x} phase diagram suggests that a mixture of AuAl and $AuAl_2$ should be present at x = 0.41. The as-deposited sample has many phases that appear to be present with mainly low intensity reflections and one large pure Al reflection as indicated in Table 2. Upon annealing, the pure Al reflection disappears, and AuAl and $AuAl_2$ are the only phases present.

At x = 0.26, we expect a mixed composition containing $AuAl_2$ and Al. The as-deposited sample contains Al, $AuAl_2$, and AuAl. Upon annealing, the $AuAl_2$ reflection dominates with a very weak reflection from Al. Al has a much lower X-ray atomic scattering factor than Au,[52] and the change in intensity cannot be used to quantify relative phase amounts. At x = 0.16, reflections from Al and $AuAl_2$ exist in both the as-deposited and annealed sample. After annealing, the reflections from $AuAl_2$ increase in intensity and sharpen. The Al reflection at 44.8 2θ also emerges upon annealing.

On the basis of the composition and phases summarized in Table 2, we examined how the dielectric constant (ε) varies as a function of the composition as well as the impact of the annealing treatment. In general, the real part (Re(ε)) becomes less negative and the imaginary part (Im(ε)) decreases for <2.6 eV and increases >2.6 eV as the atomic fraction of Au increases. However, unlike a uniform binary solid solution system such as Au−Ag,[40] the dielectric response of Au_xAl_{1-x} alloys is affected by its intermetallic compound formation and the fraction of each composition; thus, the dielectric constant does not simply continuously change as a function of composition. The Au_xAl_{1-x} system is composed of multiple intermetallic compounds, and the Drude model is not valid to describe interband transition effects. Despite the complexity, the results show interesting trends. Upon annealing, the crystallization and compound formation leads to a reduced Re(ε) in the low energy regime as observed in all samples. For the x = 0.41, 0.56, and 0.72 compositions, annealing also leads to an increase in Im(ε) indicating a higher loss in these compounds. Interestingly, for x = 0.16 and x = 0.26, the Im(ε) in the visible range is largely reduced upon annealing, which may be suitable for plasmonic applications with low damping. For x = 0.26 (primarily $AuAl_2$), the measured Im(ε) in the UV region is comparable to pure Al and lower than pure Au, while for x = 0.16, Im(ε) is generally higher than that of the x = 0.26 sample, which may be due to the coexistence of multiple phases. Furthermore, for x = 0.16 and 0.26, where $AuAl_2$ is one of the dominant phases, a peak around 2.7 eV due to the interband transition becomes prominent in the annealed sample, which is consistent with previous studies of $AuAl_2$.[53,54] The stronger interband transition peak in annealed samples is associated with an enhanced crystallinity as observed in GIXRD result, and a likely decrease in the vacancy concentration upon annealing.[54] In as-deposited films, crystal defects, phase boundaries, and vacancies introduce additional energy states around the Fermi level and induce a more complex band structure. Transitions between defect states can shift interband transitions and modify ε_2 compared to annealed films. Therefore, a decrease of these defect states may appear as a well-defined stronger interband transition peak in annealed alloy films. However, more correlated experiments and alloy band structure calculations will be performed in our future studies to further understand the underlying mechanisms. As also suggested in earlier studies, the point in which the Re(ε) crosses zero for x = 0.16 and x = 0.26 samples is at ∼2 eV, which indicates a bulk plasmon located in the visible region mediated by interband transitions in the $AuAl_2$ phase.[53]

Solid Solution of Al in Au (0.90 < x < 1.00). The solid solution region where x > 0.90 was investigated in more detail by cosputtering a gold rich sample. Specifically, the compositions that are investigated include x = 0.90, 0.93, 0.96, and 0.99. The GIXRD patterns for this region are shown in Figure 4, and the dielectric functions are presented in Figure 5. For each composition, for $x \geq 0.90$, the primary phase is the Au_xAl_{1-x} solid solution in the as-deposited sample. In the x = 0.90 and x = 0.93 compositions, the $AuAl_4$ phase precipitates

DOI: 10.1021/acscombsci.8b00091
ACS Comb. Sci. 2018, 20, 633−642

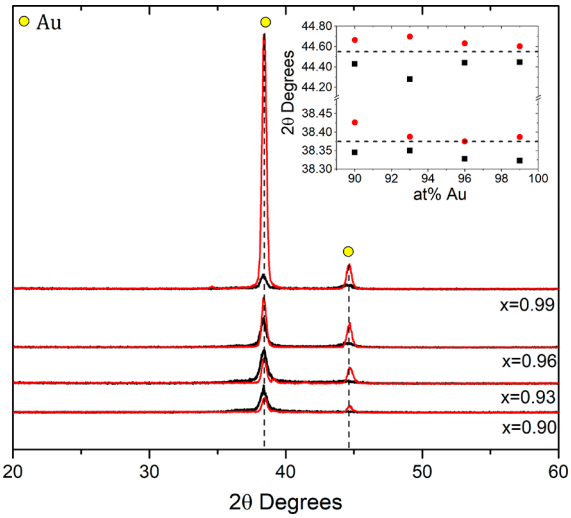

Figure 4. GIXRD results for the solid solution of Al in Au. As-deposited samples shown in black and annealed samples are shown in red. Inset shows change in peak position (2θ) as a function of %Au with pure Au peak centers shown by dashed black line.

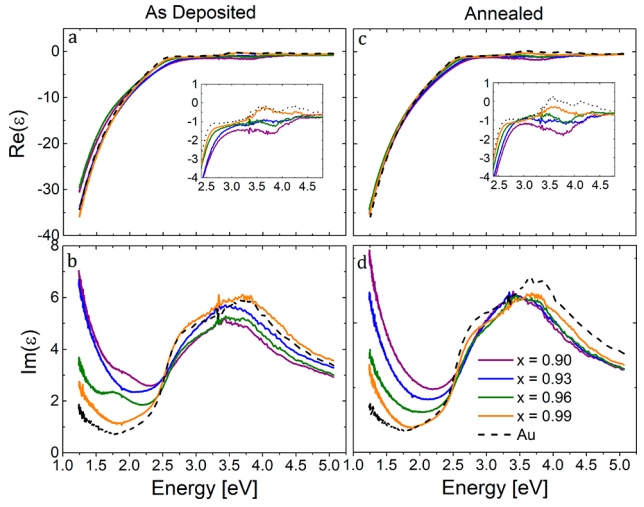

Figure 5. Dielectric function for solid solution of Al in Au. Real (a) and imaginary (b) components of the dielectric function of the as-deposited sample in the first column and the real (c) and imaginary (d) components for the annealed sample in the second column (note the inset in the real dielectric constant is a magnified view of the region for 2.4−4.8 eV).

during the anneal as observed in the XRD pattern (see Supporting Information SI1). As x increases toward pure Au, the Au reflection positions shift to higher 2θ, approaching that of pure Au, as noted in the inset of Figure 4.

Additionally, we observe a shift in peak position to larger 2θ for the annealed samples, which may be attributed to a reduction in compressive film stress. As expected, these solid solutions show an onset of the interband transition at almost the same energy as observed in pure Au. Furthermore, the imaginary dielectric function increases as the amount of Al increases, which may be attributed to defects induced by the substitutional Al atoms. These results agree well with a previous study of this region of the Au_xAl_{1-x} phase diagram.[46]

Al−$AuAl_2$ Mixed Phase (x < 0.20). In this region of the phase diagram, a mixture of Al and $AuAl_2$ is expected. The GIXRD data for this region are presented in Figure 6 and the

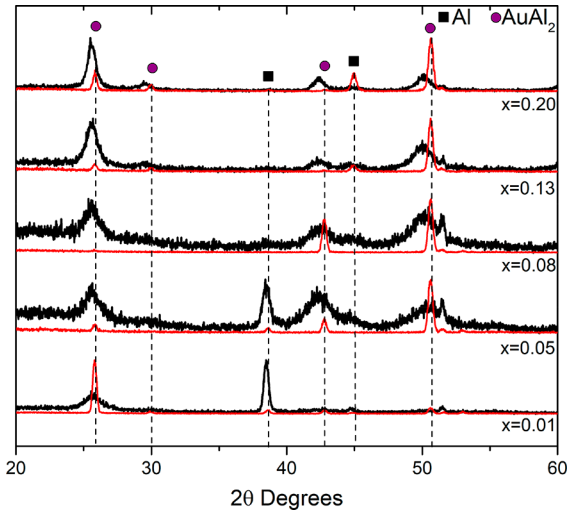

Figure 6. GIXRD data for mixed phase region Al-$AuAl_2$. As-deposited samples shown in black, while annealed samples are shown in red.

dielectric functions in Figure 7. The compositions investigated were x = 0.01, 0.05, 0.08, 0.13, and 0.20, which correspond to

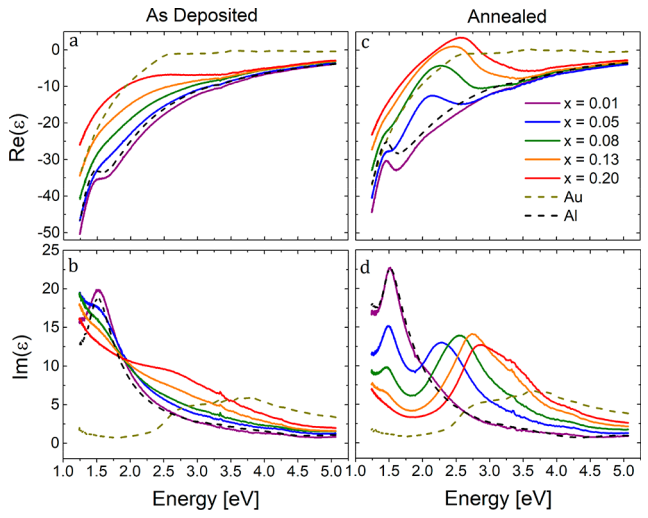

Figure 7. Dielectric function for the mixed phase region of Al-$AuAl_2$. Real (a) and imaginary (b) components of the dielectric function of the as-deposited sample in the first column and the real (c) and imaginary (d) components for the annealed sample in the second column.

approximate relative $AuAl_2$ phase amounts of 4%, 14%, 24%, 41%, and 60% $AuAl_2$. Reflections from both $AuAl_2$ and pure Al are observed in the GIXRD patterns. SEM images reveal a film texture in the annealed samples as shown in Figure 8a. EDS inspection in Figure 8b, suggests the texture is phase contrasted with brighter regions belonging to the $AuAl_2$ phase and darker regions to pure Al. SEM images of the associated as-deposited films (see Supporting Information SI2) do not have any contrast, suggestive of nanogranular morphology and likely supersaturated in each phase. This apparent phase contrast in the SEM is attributed to the grain growth/coalescence upon annealing the sample, which is also observed by the peak sharpening in the GIXRD patterns. At higher Au concentrations, there is an increase in the area of the lighter phase, consistent with an increase in the $AuAl_2$ phase.

DOI: 10.1021/acscombsci.8b00091
ACS Comb. Sci. 2018, 20, 633−642

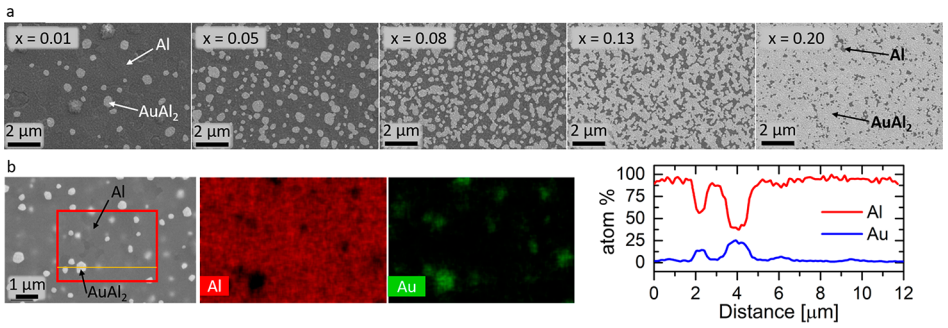

Figure 8. (a) SEM images for each composition studied, all taken at same magnification with scale bars corresponding to 2 μm. (b) SEM image and EDS mapping of a region where x = 0.01. Indicates phase contrast: bright spots are $AuAl_2$, and dark gray regions are Al (for example, labeled with arrows in x = 0.01 and 0.20). Red box corresponds to mapped area and orange line corresponds to the line scan.

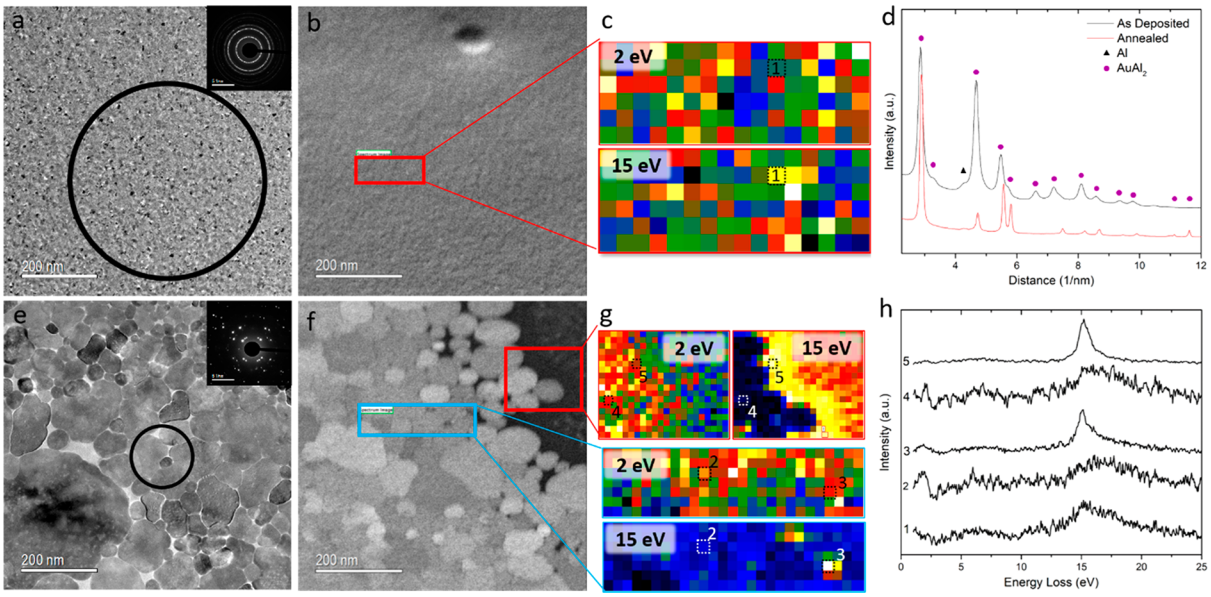

Figure 9. (a,b) As-deposited TEM image and HAADF STEM image of the as-deposited film with (c) corresponding EELS maps (2 and 15 eV). (d) Radially averaged and normalized selected area electron diffraction from a and e illustrating the presence of Al and $AuAl_2$ phases. (e–g) In situ laser annealed TEM and HAADF STEM images, respectively, and (g) corresponding EELS maps illustrating (2 and 15 eV). (h) Representative electron energy loss spectra of various positions noted in c and g. The ~2 eV peak is attributed to $AuAl_2$ and the ~15 eV peak to Al.

Due to the coexistence of the Al and $AuAl_2$ phases upon annealing, the resultant dielectric functions show features from both phases. For x = 0.01 where almost pure Al exists, ε behaves very similar to pure Al. With the increase of the $AuAl_2$ phase, the Re(ε) peak shifts to a higher energy, and the absolute value decreases until the values shift to positive at x = 0.20 as has been discussed above. In the Im(ε) part, one obvious observation is the red shift of the onset of the interband transition when the Al phase increases and may be due to an increased number of defect states in the $AuAl_2$ phase. Additionally, the onset of a second peak located at around 1.6 eV becomes obvious for the three compositions with more Al (x < 0.13). This feature is in good agreement with the reported interband transition in Al.[55] The appearance of two interband transition features in both the real and imaginary parts of the dielectric constant again reveals the coexistence of both phases.

The $Au_{0.26}Al_{0.74}$ composition was further investigated by sputtering a 20 nm film on a SiO_2 TEM membrane. The bulk plasmon peak in the EELS spectra can be used to distinguish between the $AuAl_2$ phase and the Al phase. $AuAl_2$ has a bulk plasmon at ~2 eV[53] and Al at ~15 eV.[56] The as-deposited bright field TEM and high angle annular dark field (HAADF) images are shown in Figure 9a and b, respectively, and the film is polycrystalline as revealed by the selected area electron diffraction (SAED) pattern inset in the TEM image. As expected, the radially averaged and normalized SAED (Figure 9d) contains reflections from both Al and $AuAl_2$. The HAADF STEM image of the as-deposited film, which, similarly to the SEM images of SI2 (Supporting Information), do not reveal much contrast. A representative EELS spectrum of this area is shown in Figure 9h, which features broad and low intensity peaks at 2 and 15 eV, confirming the presence of both phases with random distribution.

The sample was photothermally heated *in situ* with a 785 nm wavelength fiber coupled laser delivery system using 300 200-μs pulses at 67 mW. The laser delivery system is mounted on a three-axis nanomanipulator system for easy focusing and convenient alignment to the electron/sample coincident point. Various laser powers (up to 200 mW), pulse widths (~ 2 ns to continuous wave), and number of pulses as well as the Gaussian intensity profile (~ 5 μm radius) can all be used to study various thermal heat treatments inside the TEM and are described in detail in Wu et al.[57] Figure 9e and f are complementary bright field TEM (and SAED inset) and

DOI: 10.1021/acscombsci.8b00091
ACS Comb. Sci. 2018, 20, 633–642

HAADF STEM images of the laser treated area just outside the laser center. Figure 9g shows low loss EELS maps, and Figure 9h shows EELS spectra at various positions of the as-deposited and laser annealed film regions. At the edge of the laser spot zone, an Al rich region is formed, which is characterized by a sharp, intense low-loss EELS peak at 15 eV (Figure 9h) and illustrated in the 15 eV EELS map in bright yellow (Figure 9g). Further away from the laser center is an $AuAl_2$ rich region. The reflection corresponding to pure Al at 4.3 1/nm is greatly suppressed, and the $AuAl_2$ reflections dominate. Enhanced crystallinity is also evidenced by sharper and fewer overall spots observed in the SAED pattern of Figure 9e. The EELS spectrum here features a peak at 2 eV and a broad, low intensity peak at 15 eV, which is consistent with the $AuAl_2$ phase.

Au−Al Alloys for SERS Substrates. Gold and aluminum structures have distinct localized surface plasmon resonances (LSPR) in the visible and UV regions,[58−60] respectively, which have been taken advantage of for SERS substrates and analyses in recent years.[61,62] Additionally, there has been interest in designing gold alloys[63−67] and aluminum alloys[68,69] as SERS substrates. However, the efficacy of gold−aluminum alloys, which support LSPRs that differ from their pure metal characteristics, have not yet been studied. The SERS spectra in Figure 10 were recorded using the cosputtered Au_xAl_{1-x} alloys. Specifically, nanostrucutred Si surfaces with features in the micron size regime were coated with 200 nm Au_xAl_{1-x} (x = 0.76, 0.81, 0.88, 0.96) films, creating plasmonically active local sites. Figure 10 shows SEM images of the coated silicon substrates in plane view and tilted view, respectively. The efficacy of these plasmonic substrates for SERS based analyses was then tested through the use of the common SERS reporter molecule benezenethiol (BT). The SERS peaks at 999 cm^{-1}, 1022 cm^{-1}, 1068 cm^{-1}, and 1570 cm^{-1} are in good agreement with previously reported spectra of BT[70] and remain distinguishable from the noise for all substrates with less than 30% Al. These data highlight the need for understanding how the SERS activity is influenced by LSPR shifts upon alloying and open a path for further analysis of how alloying affects molecular absorption on the SERS substrate, and how geometric features and Au_xAl_{1-x} film thickness affect SERS activity. Furthermore, our results can be used to extrapolate the enhancement factors expected for other commonly employed SERS substrates. A gold film over nanosphere (FON) substrate,[71,72] for example, has an estimated 10^6 to 10^8 enhancement factor, suggesting that a FON substrate prepared from the alloys studied here could still yield enhancements of 10^5 to 10^7 for 30% Al composition based on the change in signal intensity shown in Figure 10.

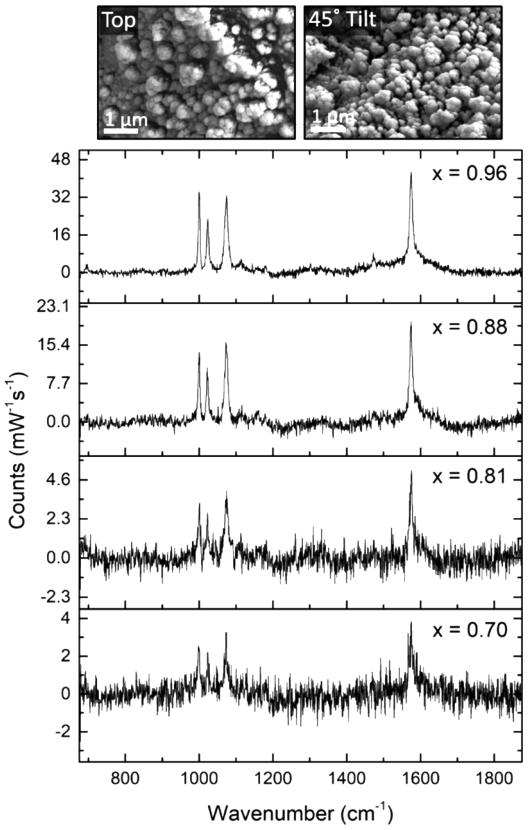

Figure 10. SERS signal for four Au−Al alloys on rough nanostructured Si surface. SEM images of nanostructured Si surface with 200 nm alloy film.

CONCLUSIONS

The structure and corresponding dielectric function for the Au_xAl_{1-x} system is studied in detail. Features in the dielectric function are correlated to phases observed in as-deposited and annealed films. The phase evolution in the annealed films is also correlated to the measured optical properties. While in some compositions metastable phases were realized in the as-deposited film, the annealed films all contained phases expected from the equilibrium phase diagram. The solid solution of Al in Au for $x > 0.9$ reveals an increase in the imaginary component of the dielectric function at low energy but otherwise behaved similarly to pure Au. In the mixed phase region of Al and $AuAl_2$, the dielectric function can effectively be tuned by altering the relative amounts of Al and $AuAl_2$ in the sample. *In situ* laser annealing of a 20 nm $Au_{0.26}Al_{0.74}$ film in the TEM revealed grain growth and coarsening of the initially nanogranular Al-AuAl2 film. The bulk plasmons of Al and $AuAl_2$ were observed with low-loss EELS as peaks at 15 and 2 eV, respectively. The as-deposited film has broad low-intensity low-loss EELS peaks relative to the larger grained annealed films. Finally, Au−Al alloys were explored as SERS substrates. In general, SERS substrates are affected by the morphology and dielectric environment,[73,74] the latter of which was the focus of our work. By keeping the morphology the same for each substrate, we are able to observe the effect of changing dielectric properties due to alloying on the relative SERS signal. Good SERS intensity was observed with up to 30% addition of Al to Au, from which we extrapolate an enhancement factor of 10^5 to 10^7 for FON substrates with these alloys. This is comparable to the 10^6 to 10^8 enhancement factor of gold FON substrates.

ASSOCIATED CONTENT

Supporting Information

The Supporting Information is available free of charge on the ACS Publications website at DOI: 10.1021/acscombsci.8b00091.

Normalized GIXRD patterns zoomed in to see Au rich peak shifts and as-deposited SEM images of Al-$AuAl_2$ sample surfaces (DOCX)

DOI: 10.1021/acscombsci.8b00091
ACS Comb. Sci. 2018, 20, 633−642

AUTHOR INFORMATION

Corresponding Author

*E-mail: prack@utk.edu.

ORCID

Robyn Collette: 0000-0002-3004-0420

Jon P. Camden: 0000-0002-6179-2692

Notes

The authors declare no competing financial interest.

ACKNOWLEDGMENTS

The authors acknowledge support from the National Science Foundation under grants NSF DMR 1709275 and 1709601. X-ray diffraction was performed at the Joint Institute for Advanced Materials (JIAM) Diffraction Facility.

REFERENCES

(1) Klein, K. L.; Melechko, A. V.; Fowlkes, J. D.; Rack, P. D.; Hensley, D. K.; Meyer, H. M.; Allard, L. F.; McKnight, T. E.; Simpson, M. L. Formation of Ultrasharp Vertically Aligned Cu−Si Nanocones by a DC Plasma Process. *J. Phys. Chem. B* **2006**, *110* (10), 4766−4771.

(2) Klein, K. L.; Melechko, A. V.; Rack, P. D.; Fowlkes, J. D.; Meyer, H. M.; Simpson, M. L. Cu−Ni composition gradient for the catalytic synthesis of vertically aligned carbon nanofibers. *Carbon* **2005**, *43* (9), 1857−1863.

(3) Guo, Q.; Noh, J. H.; Liaw, P. K.; Rack, P. D.; Li, Y.; Thompson, C. V. Density change upon crystallization of amorphous Zr−Cu−Al thin films. *Acta Mater.* **2010**, *58* (10), 3633−3641.

(4) Guan, Y.; Wang, X.; Liu, Y.; Potter, M. D.; Sorge, K. D.; Rack, P. D. Combinatorial synthesis and characterization of magnetic FexAl1−xNyO1−y thin films. *Thin Solid Films* **2008**, *516* (18), 6063−6070.

(5) Wu, Y.; Li, G.; Cherqui, C.; Bigelow, N. W.; Thakkar, N.; Masiello, D. J.; Camden, J. P.; Rack, P. D. Electron Energy Loss Spectroscopy Study of the Full Plasmonic Spectrum of Self-Assembled Au−Ag Alloy Nanoparticles: Unraveling Size, Composition, and Substrate Effects. *ACS Photonics* **2016**, *3* (1), 130−138.

(6) Wu, Y.; Fowlkes, J. D.; Rack, P. D. The optical properties of Cu-Ni nanoparticles produced via pulsed laser dewetting of ultrathin films: The effect of nanoparticle size and composition on the plasmon response. *J. Mater. Res.* **2011**, *26* (2), 277−287.

(7) Peak, J. D.; Melcher, C. L.; Rack, P. D. Combinatorial thin film sputtering investigation of cerium concentration in Lu2SiO5 scintillators. *J. Lumin.* **2010**, *130* (8), 1366−1370.

(8) Peak, J. D.; Melcher, C. L.; Rack, P. D. Combinatorial Thin Film Synthesis of Cerium Doped Scintillation Materials in the Lutetium Oxide—Silicon Oxide System. *IEEE Trans. Nucl. Sci.* **2008**, *55* (3), 1480−1483.

(9) Fowlkes, J. D.; Fitz-Gerald, J. M.; Rack, P. D. Ultraviolet emitting (Y1−xGdx)2O3−δ thin films deposited by radio frequency magnetron sputtering: Combinatorial modeling, synthesis, and rapid characterization. *Thin Solid Films* **2006**, *510* (1), 68−76.

(10) Deng, Y.; Fowlkes, J. D.; Rack, P. D.; Fitz-Gerald, J. M. Thin film rf magnetron sputtering of gadolinium-doped yttrium aluminum garnet ultraviolet emitting materials. *Opt. Mater.* **2006**, *29* (2), 183−191.

(11) Fowlkes, J. D.; Fitz-Gerald, J. M.; Rack, P. D. Ultraviolet emitting (Y1−xGdx)2O3−δ thin films deposited by radio frequency magnetron sputtering; structure-property-thin film processing relationships. *Thin Solid Films* **2007**, *515* (7), 3488−3498.

(12) Deng, Y.; Fowlkes, J. D.; Fitz-Gerald, J. M.; Rack, P. D. Combinatorial thin film synthesis of Gd-doped Y3Al5O12 ultraviolet emitting materials. *Appl. Phys. A: Mater. Sci. Process.* **2005**, *80* (4), 787−789.

(13) Jun, S.-I.; Rack, P. D.; McKnight, T. E.; Melechko, A. V.; Simpson, M. L. Electrical and microstructural characterization of molybdenum tungsten electrodes using a combinatorial thin film sputtering technique. *J. Appl. Phys.* **2005**, *97* (5), 054906.

(14) Deng, Y. P.; Guan, Y. F.; Fowlkes, J. D.; Wen, S. Q.; Liu, F. X.; Pharr, G. M.; Liaw, P. K.; Liu, C. T.; Rack, P. D. A combinatorial thin film sputtering approach for synthesizing and characterizing ternary ZrCuAl metallic glasses. *Intermetallics* **2007**, *15* (9), 1208−1216.

(15) Specht, E. D.; Rack, P. D.; Rar, A.; Pharr, G. M.; George, E. P.; Fowlkes, J. D.; Hong, H.; Karapetrova, E. Metastable phase evolution and grain growth in annealed nanocrystalline Cr−Fe−Ni films. *Thin Solid Films* **2005**, *493* (1), 307−312.

(16) Rar, A.; Frafjord, J. J.; Fowlkes, J. D.; Specht, E. D.; Rack, P. D.; Santella, M. L.; Bei, H.; George, E. P.; Pharr, G. M. PVD synthesis and high-throughput property characterization of Ni−Fe−Cr alloy libraries. *Meas. Sci. Technol.* **2005**, *16* (1), 46.

(17) Nagase, T.; Anada, S.; Rack, P. D.; Noh, J. H.; Yasuda, H.; Mori, H.; Egami, T. MeV electron-irradiation-induced structural change in the bcc phase of Zr−Hf−Nb alloy with an approximately equiatomic ratio. *Intermetallics* **2013**, *38*, 70−79.

(18) Nagase, T.; Anada, S.; Rack, P. D.; Noh, J. H.; Yasuda, H.; Mori, H.; Egami, T. Electron-irradiation-induced structural change in Zr−Hf−Nb alloy. *Intermetallics* **2012**, *26*, 122−130.

(19) Li, G.; Zhou, L.; Guevarra, D.; Suram, S. K.; Shinde, A.; Li, G.; Zhou, L.; Guevarra, D.; Suram, S. K.; Toma, F. M.; Yan, Q.; Haber, J. A.; Neaton, J. B.; Gregoire, J. M.; Shinde, A. The role of the CeO 2 /BiVO 4 interface in optimized Fe−Ce oxide coatings for solar fuels photoanodes. *J. Mater. Chem. A* **2016**, *4* (37), 14356−14363.

(20) Jeon, M. K.; Lee, C. H.; Park, G. I.; Kang, K. H. Combinatorial search for oxygen reduction reaction electrocatalysts: A review. *J. Power Sources* **2012**, *216*, 400−408.

(21) Yang, K.; Bedenbaugh, J.; Li, H.; Peralta, M.; Bunn, J. K.; Lauterbach, J.; Hattrick-Simpers, J. Development of a High-Throughput Methodology for Screening Coking Resistance of Modified Thin-Film Catalysts. *ACS Comb. Sci.* **2012**, *14* (6), 372−377.

(22) König, D.; Richter, K.; Siegel, A.; Mudring, A.-V.; Ludwig, A. High-Throughput Fabrication of Au−Cu Nanoparticle Libraries by Combinatorial Sputtering in Ionic Liquids. *Adv. Funct. Mater.* **2014**, *24* (14), 2049−2056.

(23) Liu, Y.; Padmanabhan, J.; Cheung, B.; Liu, J.; Chen, Z.; Scanley, B. E.; Wesolowski, D.; Pressley, M.; Broadbridge, C. C.; Altman, S.; Schwarz, U. D.; Kyriakides, T. R.; Schroers, J. Combinatorial development of antibacterial Zr-Cu-Al-Ag thin film metallic glasses. *Sci. Rep.* **2016**, *6*, 26950.

(24) Alexandrakis, V.; Kusne, A. G.; Gao, T.; Fackler, S. W.; König, D.; Kramer, M. J.; Stasak, D.; Lopez, K.; Zayac, B.; Mehta, A.; Ludwig, A.; Takeuchi, I. Combinatorial study of Fe-Co-V hard magnetic thin films. *Sci. Technol. Adv. Mater.* **2017**, *18* (1), 231−238.

(25) Suchoski, R.; Fackler, S.; Zhang, Y.; Pan, X.; Jin, K.; Greene, R. L.; Takeuchi, I. Combinatorial search of superconductivity in Fe-B composition spreads. *APL Mater.* **2013**, *1* (4), 042101.

(26) Liu, J.; Liu, Y.; Gong, P.; Li, Y.; Moore, K. M.; Scanley, E.; Walker, F.; Broadbridge, C. C.; Schroers, J. Combinatorial exploration of color in gold-based alloys. *Gold Bull.* **2015**, *48* (3), 111−118.

(27) Gong, C.; Leite, M. S. Noble Metal Alloys for Plasmonics. *ACS Photonics* **2016**, *3* (4), 507−513.

(28) Han, Y.; Siol, S.; Zhang, Q.; Zakutayev, A. Optoelectronic Properties of Strontium and Barium Copper Sulfides Prepared by Combinatorial Sputtering. *Chem. Mater.* **2017**, *29* (19), 8239−8248.

(29) McCluskey, P. J.; Xiao, K.; Gregoire, J. M.; Dale, D.; Vlassak, J. J. Application of in-situ nano-scanning calorimetry and X-ray diffraction to characterize Ni−Ti−Hf high-temperature shape memory alloys. *Thermochim. Acta* **2015**, *603*, 53−62.

(30) Fioretti, A. N.; Zakutayev, A.; Moutinho, H.; Melamed, C.; Perkins, J. D.; Norman, A. G.; Al-Jassim, M.; Toberer, E. S.; Tamboli, A. C. Combinatorial insights into doping control and transport properties of zinc tin nitride. *J. Mater. Chem. C* **2015**, *3* (42), 11017−11028.

(31) Chang, K. S.; Green, M. L.; Suehle, J.; Vogel, E. M.; Xiong, H.; Hattrick-Simpers, J.; Takeuchi, I.; Famodu, O.; Ohmori, K.; Ahmet,

DOI: 10.1021/acscombsci.8b00091
ACS Comb. Sci. 2018, 20, 633−642

P.; Chikyow, T.; Majhi, P.; Lee, B. H.; Gardner, M. Combinatorial study of Ni−Ti−Pt ternary metal gate electrodes on HfO2 for the advanced gate stack. *Appl. Phys. Lett.* **2006**, *89* (14), 142108.
(32) Motemani, Y.; McCluskey, P. J.; Zhao, C.; Tan, M. J.; Vlassak, J. J. Analysis of Ti−Ni−Hf shape memory alloys by combinatorial nanocalorimetry. *Acta Mater.* **2011**, *59* (20), 7602−7614.
(33) Green, M. L.; Takeuchi, I.; Hattrick-Simpers, J. R. Applications of high throughput (combinatorial) methodologies to electronic, magnetic, optical, and energy-related materials. *J. Appl. Phys.* **2013**, *113* (23), 231101.
(34) Gebhardt, T.; Music, D.; Takahashi, T.; Schneider, J. M. Combinatorial thin film materials science: From alloy discovery and optimization to alloy design. *Thin Solid Films* **2012**, *520* (17), 5491−5499.
(35) Mao, S. S.; Burrows, P. E. Combinatorial screening of thin film materials: An overview. *Journal of Materiomics* **2015**, *1* (2), 85−91.
(36) Potyrailo, R.; Rajan, K.; Stoewe, K.; Takeuchi, I.; Chisholm, B.; Lam, H. Combinatorial and High-Throughput Screening of Materials Libraries: Review of State of the Art. *ACS Comb. Sci.* **2011**, *13* (6), 579−633.
(37) Blaber, M. G.; Arnold, M. D.; Ford, M. J. A review of the optical properties of alloys and intermetallics for plasmonics. *J. Phys.: Condens. Matter* **2010**, *22* (14), 143201.
(38) Gao, C.; Hu, Y.; Wang, M.; Chi, M.; Yin, Y. Fully Alloyed Ag/Au Nanospheres: Combining the Plasmonic Property of Ag with the Stability of Au. *J. Am. Chem. Soc.* **2014**, *136* (20), 7474−7479.
(39) Hambrock, J.; Schröter, M. K.; Birkner, A.; Wöll, C.; Fischer, R. A. Nano-Brass: Bimetallic Copper/Zinc Colloids by a Nonaqueous Organometallic Route Using [Cu(OCH(Me)CH2NMe2)2] and Et2Zn as Precursors. *Chem. Mater.* **2003**, *15* (22), 4217−4222.
(40) Peña-Rodríguez, O.; Caro, M.; Rivera, A.; Olivares, J.; Perlado, J. M.; Caro, A. Optical properties of Au-Ag alloys: An ellipsometric study. *Opt. Mater. Express* **2014**, *4* (2), 403−410.
(41) Yang, G.; Fu, X.; Zhou, J. Dielectric properties of the silver-copper alloy films deposited by magnetron sputtering. *J. Opt. Soc. Am. B* **2013**, *30* (2), 282−287.
(42) Amendola, V.; Pilot, R.; Frasconi, M.; Marago, O. M.; Iatì, M. A. Surface plasmon resonance in gold nanoparticles: a review. *J. Phys.: Condens. Matter* **2017**, *29* (20), 203002.
(43) Knight, M. W.; King, N. S.; Liu, L.; Everitt, H. O.; Nordlander, P.; Halas, N. J. Aluminum for Plasmonics. *ACS Nano* **2014**, *8* (1), 834−840.
(44) Keast, V. J.; Zwan, B.; Supansomboon, S.; Cortie, M. B.; Persson, P. O. Å. AuAl2 and PtAl2 as potential plasmonic materials. *J. Alloys Compd.* **2013**, *577*, 581−586.
(45) Keast, V. J.; Barnett, R. L.; Cortie, M. B. First principles calculations of the optical and plasmonic response of Au alloys and intermetallic compounds. *J. Phys.: Condens. Matter* **2014**, *26* (30), 305501.
(46) De Silva, K. S. B.; Keast, V. J.; Cortie, M. B. Effect of Al additions on the optical properties of Au α-phase. *J. Alloys Compd.* **2016**, *679*, 225−230.
(47) Murray, J. L.; Okamoto, H.; Massalski, T. B. The Al−Au (Aluminum-gold) system. *Bull. Alloy Phase Diagrams* **1987**, *8* (1), 20−30.
(48) Bearden, J. A. X-Ray Wavelengths. *Rev. Mod. Phys.* **1967**, *39* (1), 78−124.
(49) Li, M.; Li, C.; Wang, F.; Luo, D.; Zhang, W. Thermodynamic assessment of the Al−Au system. *J. Alloys Compd.* **2004**, *385* (1), 199−206.
(50) Xu, C.; Sritharan, T.; Mhaisalkar, S. G. Thin film aluminum−gold interface interactions. *Scr. Mater.* **2007**, *56* (6), 549−552.
(51) Majni, G.; Nobili, C.; Ottaviani, G.; Costato, M.; Galli, E. Gold-aluminum thin-film interactions and compound formation. *J. Appl. Phys.* **1981**, *52* (6), 4047−4054.
(52) Chantler, C. T. Theoretical Form Factor, Attenuation, and Scattering Tabulation for Z = 1−92 from E = 1−10 eV to E = 0.4−1.0 MeV. *J. Phys. Chem. Ref. Data* **1995**, *24* (1), 71−643.
(53) Keast, V. J.; Birt, K.; Koch, C. T.; Supansomboon, S.; Cortie, M. B. The role of plasmons and interband transitions in the color of AuAl2, AuIn2, and AuGa2. *Appl. Phys. Lett.* **2011**, *99* (11), 111908.
(54) Keast, V. J.; Wallace, J. W.; Wrightson, C. J.; Tai, M.; Gentle, A.; Arnold, M. D.; Cortie, M. B. The effect of vacancies on the optical properties of AuAl 2. *J. Phys.: Condens. Matter* **2015**, *27* (50), 505501.
(55) Petri, E.; Otto, A. Direct Nonvertical Interband and Intraband Transitions in Al. *Phys. Rev. Lett.* **1975**, *34* (20), 1283−1286.
(56) Egerton, R. F. *Electron Energy-Loss Spectroscopy in the Electron Microscope*; Springer Science+Business Media, Boston, MA, 2011.
(57) Wu, Y. L., Moore, T. M.; Magel, G. A.; Garfinkel, D. A.; Camden, J. P.; Stanford, M. G.; Duscher, G.; Rack, P. D.; Chen, Z. Exploring Photothermal Pathways via In Situ Laser Heating in the Transmission Electron Microscope: Recrystallization, Grain Growth, Phase Separation and Dewetting in $Ag_{0.5}Ni_{0.5}$ Thin Films. *Microscopy and Microanalysis*. Submitted May 2018.
(58) Langhammer, C.; Schwind, M.; Kasemo, B.; Zorić, I. Localized Surface Plasmon Resonances in Aluminum Nanodisks. *Nano Lett.* **2008**, *8* (5), 1461−1471.
(59) Chan, G. H.; Zhao, J.; Schatz, G. C.; Van Duyne, R. P. Localized Surface Plasmon Resonance Spectroscopy of Triangular Aluminum Nanoparticles. *J. Phys. Chem. C* **2008**, *112* (36), 13958−13963.
(60) Zorić, I.; Zäch, M.; Kasemo, B.; Langhammer, C. Gold, Platinum, and Aluminum Nanodisk Plasmons: Material Independence, Subradiance, and Damping Mechanisms. *ACS Nano* **2011**, *5* (4), 2535−2546.
(61) Jahn, M.; Patze, S.; Hidi, I. J.; Knipper, R.; Radu, A. I.; Mühlig, A.; Yüksel, S.; Peksa, V.; Weber, K.; Mayerhöfer, T.; Cialla-May, D.; Popp, J. Plasmonic nanostructures for surface enhanced spectroscopic methods. *Analyst* **2016**, *141* (3), 756−793.
(62) Tian, S.; Neumann, O.; McClain, M. J.; Yang, X.; Zhou, L.; Zhang, C.; Nordlander, P.; Halas, N. J. Aluminum Nanocrystals: A Sustainable Substrate for Quantitative SERS-Based DNA Detection. *Nano Lett.* **2017**, *17* (8), 5071−5077.
(63) Huang, J.; Zhu, Y.; Lin, M.; Wang, Q.; Zhao, L.; Yang, Y.; Yao, K. X.; Han, Y. Site-Specific Growth of Au−Pd Alloy Horns on Au Nanorods: A Platform for Highly Sensitive Monitoring of Catalytic Reactions by Surface Enhancement Raman Spectroscopy. *J. Am. Chem. Soc.* **2013**, *135* (23), 8552−8561.
(64) Lee, Y. W.; Kim, N. H.; Lee, K. Y.; Kwon, K.; Kim, M.; Han, S. W. Synthesis and Characterization of Flower-Shaped Porous Au−Pd Alloy Nanoparticles. *J. Phys. Chem. C* **2008**, *112* (17), 6717−6722.
(65) Fan, M.; Lai, F.-J.; Chou, H.-L.; Lu, W.-T.; Hwang, B.-J.; Brolo, A. G. Surface-enhanced Raman scattering (SERS) from Au:Ag bimetallic nanoparticles: the effect of the molecular probe. *Chemical Science* **2013**, *4* (1), 509−515.
(66) Liu, Z.; Yang, Z.; Peng, B.; Cao, C.; Zhang, C.; You, H.; Xiong, Q.; Li, Z.; Fang, J. Highly Sensitive, Uniform, and Reproducible Surface-Enhanced Raman Spectroscopy from Hollow Au-Ag Alloy Nanourchins. *Adv. Mater.* **2014**, *26* (15), 2431−2439.
(67) Jiang, Z.; Zhang, Q.; Zong, C.; Liu, B.-J.; Ren, B.; Xie, Z.; Zheng, L. Cu−Au alloy nanotubes with five-fold twinned structure and their application in surface-enhanced Raman scattering. *J. Mater. Chem.* **2012**, *22* (35), 18192−18197.
(68) Shi, T.; Kong, J.; Wang, X.; Li, X. Preparation of multifunctional Al-Mg alloy surface with hierarchical micro/nanostructures by selective chemical etching processes. *Appl. Surf. Sci.* **2016**, *389*, 335−343.
(69) Cherepy, N. J.; Shen, T. H.; Esposito, A. P.; Tillotson, T. M. Characterization of an effective cleaning procedure for aluminum alloys: surface enhanced Raman spectroscopy and zeta potential analysis. *J. Colloid Interface Sci.* **2005**, *282* (1), 80−86.
(70) Joo, T. H.; Kim, M. S.; Kim, K. Surface-enhanced Raman scattering of benzenethiol in silver sol. *J. Raman Spectrosc.* **1987**, *18* (1), 57−60.
(71) Farcau, C.; Astilean, S. Mapping the SERS Efficiency and Hot-Spots Localization on Gold Film over Nanospheres Substrates. *J. Phys. Chem. C* **2010**, *114* (27), 11717−11722.

DOI: 10.1021/acscombsci.8b00091
ACS Comb. Sci. 2018, 20, 633−642

(72) Baia, L.; Baia, M.; Popp, J.; Astilean, S. Gold Films Deposited over Regular Arrays of Polystyrene Nanospheres as Highly Effective SERS Substrates from Visible to NIR. *J. Phys. Chem. B* **2006**, *110* (47), 23982−23986.
(73) Le Ru, E. C.; Blackie, E.; Meyer, M.; Etchegoin, P. G. Surface Enhanced Raman Scattering Enhancement Factors: A Comprehensive Study. *J. Phys. Chem. C* **2007**, *111* (37), 13794−13803.
(74) Camden, J. P.; Dieringer, J. A.; Zhao, J.; Van Duyne, R. P. Controlled Plasmonic Nanostructures for Surface-Enhanced Spectroscopy and Sensing. *Acc. Chem. Res.* **2008**, *41* (12), 1653−1661.

DOI: 10.1021/acscombsci.8b00091
ACS Comb. Sci. 2018, 20, 633−642